Signatures of electronic ordering in transport in graphene flat bands

Archisman Panigrahi [*] and Leonid Levitov

Department of Physics, Massachusetts Institute of Technology, Cambridge, Massachusetts 02139, USA

Recently, a wide family of electronic orders was unveiled in graphene flat bands, such as spin- and valley-polarized phases as well as nematic momentum-polarized phases, stabilized by exchange interactions via a generalized Stoner mechanism. Momentum polarization involves orbital degrees of freedom and is therefore expected to impact resistivity in a way that is uniquely sensitive to the ordering type. Under pocket polarization, carrier distribution shifts in k space and samples the band mass in regions defined by the displaced momentum distribution. This makes transport coefficients sensitive to pocket polarization, resulting in the Ohmic resistivity decreasing with temperature. In addition, it leads to current switching and hysteresis under strong E field. Being robust in the presence of electron-phonon scattering, this behavior can serve as a telltale sign of pocket polarization order. The fast timescale and low dissipation of the switching cycle may be advantageous for highly applicable memory-dependent resistors, i.e., memristors.

I. INTRODUCTION

Recent experiments reported on a cascade of strongly correlated phases in moiré graphene multilayers [1–16] as well as their non-moiré counterparts [17–24], where the electronic properties can be tuned by altering the external displacement field (D) and the electron density (n). Moiré graphene hosts flat minibands with high density of states, where the effects of electronic interactions become significant [25–47]. Likewise, in non-moiré stacked graphene the displacement field opens up a gap and the resulting bands become remarkably flat near their extrema, giving rise to similar interaction-driven ordered phases [48–64]. To minimize the exchange energy, the electrons spontaneously break the combined SU(4) symmetries in the spin-valley degrees of freedom, giving rise to valley-polarized and spin-polarized ferromagnetic orders [3–5,7–11,36–41,50–52,55]. Electronic ordering of a different kind can arise in non-moiré graphene multilayers when electrons partially fill the pockets induced by trigonal warping of carrier bands near the K and K' points. Such carrier flocking in momentum space, driven by electron exchange interaction and described by Stoner-type instability, produces nematic momentum-polarized orders where only some of the pockets remain populated [22,23,61]. Upon temperature increasing, the ordering disappears through what is currently believed to be a continuous phase transition.

Several different techniques have been employed to probe electronic orders at low temperatures. Phase boundaries between different ordered phases can be probed by electronic compressibility measurements, which capture the change in density of states at the Fermi surface, across the phase transition [18,20,22]. The low-temperature momentum-polarized, spin-polarized, and valley-polarized orders can be identified by quantum oscillations measurements [19], which

reveal the spin/valley degeneracy and the Fermi surface geometry.

In comparison, the signatures of ordering in the temperature dependence of transport coefficients have received relatively little attention. The only transport signature explored so far, which distinguishes symmetry-broken phases, was the anomalous Hall effect observed in the valley-polarized phase at low temperature, which disappear at elevated temperatures [4,21,42]. In that, the K and K' valleys, which have opposite signs of Berry curvature, give rise to an anomalous Hall response resulting from broken time-reversal symmetry.

Motivated by recent findings [65], in this work we consider the momentum-polarized order perturbed by a DC electric current, both in the Ohmic regime (linear field-current response) and in the non-Ohmic (nonlinear response) regime. Instead of the Berry curvature, we focus on the band dispersion and its dependence on the pocket-polarization ordering. As we will see, under such ordering, carrier distribution shifts in k space and samples the band curvature in regions defined by the displaced Fermi sea. This behavior makes transport coefficients sensitive to pocket polarization and leads to a unique signature of ordering—the negative temperature dependence of resistivity below the order-disorder transition. Namely, rising temperatures, despite increasing electronic disorder, drive the system into a more conducting state. This behavior originates from an interplay between exchange interactions that make carriers aggregate in Fermi pockets and thermal activation that excites carriers out of the Fermi pockets.

Furthermore, under the application of a strong electric field, the momentum-polarized phase can exhibit history dependence and switching of pocket polarization. This behavior is illustrated in Fig. 2, which displays the results of a microscopic analysis developed in Sec. VI. The resulting current switching may serve as an experimental test for discerning the proposed mechanism of negative temperature dependence of resistivity from alternative mechanisms. Similar switching behavior has been observed in recent experiments [4,15,66]

*archi137@mit.edu

in twisted bilayer graphene, transition metal dichalcogenides, and twisted trilayer graphene. It has been studied theoretically for magic-angle twisted bilayer graphene [67].

The switching mechanism in these systems does not involve any movement of impurities, nor does it involve any movement of electrons in the real space. Instead, it is driven by carrier distribution switching between different pockets in momentum space. Consequently, the switching timescale will be very fast, which opens up the possibility of using these systems as memory-dependent resistors, i.e., memristors [68]. Moreover, since the switching is observed at relatively small currents (nano-Ampéres) [15], the dissipation per switching cycle is expected to be small, potentially leading to highly efficient memristors.

II. TRANSPORT ANOMALIES DUE TO POCKET POLARIZATION ORDERING

The system in question, where a phase transition alters the geometry and symmetry of the Fermi sea, features band dispersion which is uniquely sensitive to carrier momentum distribution. Namely, the phase transition changes the band curvature $m_{k_i k_j}^{-1} = \partial^2 \varepsilon_{\boldsymbol{k}} / \partial k_i \partial k_j$ defined by the part of the band occupied by carriers,

$$C(T) = \left\langle \frac{\partial^2 \varepsilon_{\boldsymbol{k}}}{\partial k_x^2} \right\rangle_T = \frac{1}{n} \sum_{\boldsymbol{k},\sigma} \frac{\partial^2 \varepsilon_{\boldsymbol{k},\sigma}}{\partial k_x^2} f_{\boldsymbol{k},\sigma}, \qquad (1)$$

where $f_{\boldsymbol{k},\sigma}$ is momentum distribution and $\varepsilon_{\boldsymbol{k}}$ is band dispersion, which in itself depends, via exchange interaction, on $f_{\boldsymbol{k},\sigma}$. (Here $n = \sum_{\boldsymbol{k},\sigma} f_{\boldsymbol{k},\sigma}$ is carrier density.) As illustrated in Fig. 1(a) and 1(b), different parts of a two-pocket carrier band have curvature of opposite signs and, therefore, give opposite-sign contributions to $C(T)$.

As we will see, the changes in $C(T)$ driven by ordering translate into a characteristic T dependence of the resistivity. We will outline a mechanism through which the resistivity in the ordered phase at low temperature can be higher than that of the disordered phase at a higher temperature. In other words, we argue that the resistivity can decrease with rising temperature, as the ordered phase melts. Negative temperature dependence, $d\rho/dT < 0$, stands in contrast with the sign of temperature dependence typically seen in metals due to carrier scattering by lattice vibrations. The low characteristic temperature at which it is expected to occur as well as the sign make the negative $d\rho/dT$ a telltale sign of pocket-polarization ordering.

The mechanism leading to negative $d\rho/dT$ is illustrated in Fig. 1. In Boltzmann transport theory [69] the dc Ohmic conductivity is given by the expression,

$$\sigma_{xx}(T) = \sum_{\boldsymbol{k},\sigma} \frac{e^2 \tau(T)}{\hbar^2} \frac{\partial^2 \varepsilon_{\boldsymbol{k},\sigma}}{\partial k_x^2} f_{\boldsymbol{k},\sigma} = \frac{ne^2 \tau(T)}{\hbar^2} C(T), \qquad (2)$$

where $f_{\boldsymbol{k},\sigma}$ is the momentum distribution, $\sum_{\boldsymbol{k}}$ is a shorthand for $\int \frac{d^2\boldsymbol{k}}{(2\pi)^2}$, and, for simplicity, the relaxation timescale τ is assumed to be momentum independent. Clearly, Eq. (2) implies that between two phases with comparable τ values, the one with greater average band curvature $C(T)$ will have a smaller resistivity.
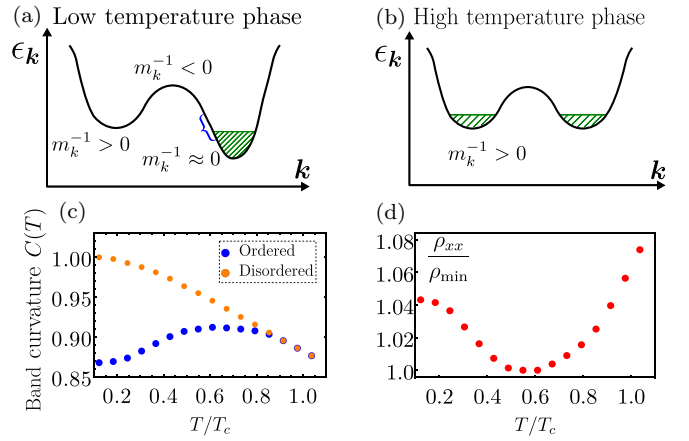
FIG. 1. (a), (b) Pocket-polarized and unpolarized states for a double-well one-dimensional (1D) model, Eq. (11). Marked are regions in which the band curvature $m_k^{-1} = \partial^2 \varepsilon_k / \partial k^2$ is positive, negative, and close to zero. The pocket-polarized carrier distribution shifts in k space and samples the band curvature, Eq. (1), in regions within the displaced momentum distribution. This makes transport coefficients sensitive to pocket polarization, resulting in ohmic resistance decreasing with temperature (see text). (c) Temperature dependence of the occupancy-weighted band curvature $C(T)$, Eq. (1), for the ordered states (blue) and the metastable disordered states (orange). (d) The resulting resistivity temperature dependence is nonmonotonic. Initially, resistivity drops due to the increase in the band curvature of the ordered phase. At higher temperature the phonon scattering grows, and the resistivity increases linearly. Parameter values used are given in Sec. V.

The quantity $\varepsilon_{\boldsymbol{k},\sigma}$ in Eq. (2) denotes the band dispersion modified by interactions, and $f_{\boldsymbol{k},\sigma}$ is the Fermi function for this band dispersion. Under mean-field theory developed below, the pocket-asymmetric part of the momentum distribution $f_{\boldsymbol{k},\sigma}$ plays the role of the order parameter describing pocket polarization. The energy $\varepsilon_{\boldsymbol{k},\sigma}$ depends on $f_{\boldsymbol{k},\sigma}$ and the noninteracting band dispersion $\varepsilon_{\boldsymbol{k}}^0$ as

$$\varepsilon_{\boldsymbol{k},\sigma} = \varepsilon_{\boldsymbol{k}}^0 - \sum_{\boldsymbol{k}' \neq \boldsymbol{k}} V(\boldsymbol{k} - \boldsymbol{k}') f_{\boldsymbol{k}',\sigma}, \qquad (3)$$

where $f_{\boldsymbol{k},\sigma}$ is given by a Fermi distribution for the band dispersion modified by interactions,

$$f_{\boldsymbol{k},\sigma} = \frac{1}{e^{\beta(\varepsilon_{\boldsymbol{k},\sigma} - \mu)} + 1}, \qquad (4)$$

and $V(\boldsymbol{k} - \boldsymbol{k}')$ represents the electronic interactions (see Sec. IV). Equations (3) and (4), solved self-consistently, describe carrier momentum distribution in the ground state in the presence of exchange interactions. When interactions are strong enough, the momentum distribution becomes pocket asymmetric at low temperature, as illustrated in Figs. 1 and 2. The occurrence of multiple fixed points for the self-consistent solution of these equations is a signature of a pocket symmetry breaking instability towards pocket polarization order. Upon temperature increasing, the solution undergoes a transition to a disordered pocket-symmetric state.

We now discuss reasons for which the average occupancy-weighted band curvature, Eq. (1), can be lower in the
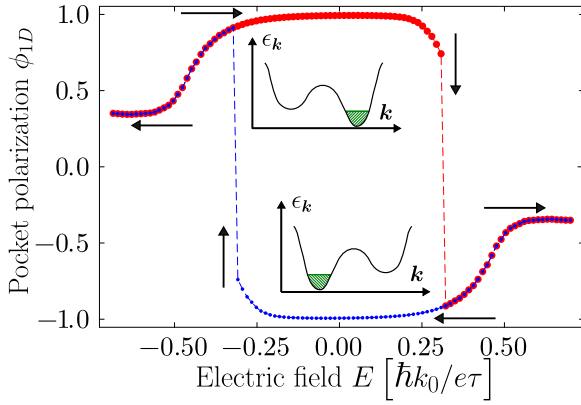
FIG. 2. Pocket-polarization switching and history dependence of the dynamics under the action of an electric field for the model illustrated in Fig. 1. As discussed in Sec. VI, the initial state is the equilibrium state polarized in the right (left) pocket for the red (blue) curve. For each value of electric field E, we self-consistently determine the steady state, and plot the pocket polarization $\phi_{1D} = (n_R - n_L)/(n_R + n_L)$ against the (dimensionless) electric field. The right and left pocket-polarized steady states are pictured inside the hysteresis loop. For the right pocket-polarized initial state (red curve), for positive electric fields, the Fermi sea shifts to the $-\hat{k}_x$ direction, and the distribution switches to the left pocket at a finite electric field. No such switching occurs when the electric field is swept in the other direction. The opposite effect occurs for the left-pocket-polarized initial state (blue curve). The black arrows show the direction of switching of the steady state when the electric field is swept.

low-temperature phase than that in the corresponding high-temperature disordered phase, thus leading to resistivity decreasing with temperature. As an illustration, consider the momentum-polarized to momentum-unpolarized transition, focusing, for simplicity, on the pocket-polarized order in a single valley with a single spin species. Bilayer graphene hosts three pockets (or four pockets, at small enough displacement field) induced by trigonal warping near its $\bm{K}/\bm{K}'$ points [70]. The regions in k space where these pockets merge have a negative band curvature (holelike), whereas the minima of the pockets have a positive band curvature. At low temperature, the ordered phase with a high enough electron density will feature a band filled up to the neck of a single pocket [Fig. 1(a)]. The band curvature of this pocket near the chemical potential will be much smaller than that near the pocket bottom. As temperature is increased, the electrons will be thermally excited to (i) high-energy states within the same pocket, which either have a positive band curvature with smaller magnitude, or a curvature with negative sign, and, (ii) the low-energy states of the previously empty pocket, where the band curvature is positive and has relatively large magnitude. Clearly, there will be a competition between the two effects. When the electron density is high enough such that the chemical potential at low temperature is close to the bottom of the empty pocket, the second effect wins due to the high density of states, and the occupancy-averaged band curvature increases with temperature.

Experimentally, such an effect may occur on the high-density side of the momentum-polarized phase in the n-D

phase diagram, D being the displacement field. The density needs to be such that the Fermi energy of the filled pocket is close to the bottom of the empty pocket, so that due to thermal excitations, electrons will be excited to the bottom of the empty pocket, decreasing the average curvature (of course, there will be a competition between the higher energy states of the partially filled pocket and the bottom states of the empty pocket). To the contrary, when the density is low, the distance between the Fermi energy at the filled pocket and the bottom of the empty pocket may be too large for thermal excitations to excite the electrons to the bottom of the empty pocket.

At temperatures below the Bloch-Grüneisen temperature [69,71,72], phonons are not yet thermally activated, so the carrier momentum relaxation timescale $\tau(T)$ remains almost temperature independent. At such temperatures, the resistivity will primarily depend on the band curvature. As temperature varies, the resistivity initially decreases with rising temperature as the average band curvature increases due to gradual melting of the ordered phase. Eventually, the resistance will begin to grow with temperature as the phonons become thermally activated. In Sec. V we establish this effect with two microscopic models that resemble the pockets in the bilayer graphene band structure [see Figs. 1(d) and 4(c)].

It is instructive to compare the resulting temperature dependence, which is fairly strong, to various scenarios discussed in the literature. Phase transitions in metals of first order usually result in resistance discontinuity at the phase transition but little T dependence away from it. Phase transitions of second order in general lead to strong order parameter fluctuations at T above and below the transition, and a singularity at the transition. These fluctuations, however, are of a long-wavelength character, and, as a result, do not produce a strong T dependence of transport cross-section and resistivity [73]. In contrast, electronic ordering in graphene flat bands discussed here impacts carrier scattering at large angles, i.e., in a wide range of transferred momenta k. This makes resistivity sensitive to the ordering type, giving rise to the T dependence discussed below.

We also comment on several effects due to electron interactions that can potentially result in a negative temperature dependence of resistivity, $d\rho/dT < 0$. Some years ago, ultra-clean silicon MOSFETs were found to exhibit negative T dependence of resistivity. A number of mechanisms to explain this behavior have been proposed. Those included the Coulomb scattering cross-section weakening at a higher temperature [74], an effect that leads to a decrease in the disorder scattering rate. Other explanations focused on the effects due to the presence of charge traps and the Altshuler-Aronov-type interaction effects [75–77].

Furthermore, a very different physics resulting in a negative T dependent resistivity was proposed for clean metals, where carrier collisions can result in hydrodynamic transport, wherein electrons undergoing two-body collisions behave as a viscous fluid [78]. Electron hydrodynamics can naturally lead to resistivity that decreases with temperature. Later, however, it has been argued that the actual behavior is more nuanced [79]. Namely, correlated electron systems in a slowly varying disorder potential were predicted to show resistivity with a growing T dependence, an effect arising due to the interplay of heat conduction and thermoelectric effects. More recently,

however, hydrodynamic transport in clean electron systems with sharp boundaries was confirmed to result in a negative temperature dependence of resistivity [80,81]. The prediction of hydrodynamic resistivity decreasing with temperature is supported by recent measurements [82,83].

This behavior must therefore be accounted for in delineating mechanisms leading to a negative T dependence in realistic systems. We note in that regard that there are several qualitative aspects of the pocket-polarization mechanism for negative temperature dependence of resistivity, $d\rho/dT < 0$, which make it distinct from other known mechanisms. One is its lack of sensitivity to the cleanness of the system. This stands in contrast to electron hydrodynamics, which requires the electron system to be ultraclean. Another is that it is tied to temperature at which the pocket-polarization phase transition occurs. Lastly, as discussed below, pocket polarization order gives rise to a switching behavior of the nonlinear I-V dependence, which coexists with the negative temperature dependence of resistivity. These properties occurring together will provide clear signatures of transport anomalies due to pocket-polarization instability.

III. PHENOMENOLOGICAL PICTURE

Temperature dependence of transport coefficients near pocket-polarization ordering is governed by competition of two distinct effects. First, pocket polarization results in carrier redistribution in k space. As temperature varies, carriers sample different parts of the band, producing temperature-dependent resistivity. Furthermore, because of exchange interactions, the band dispersion and band curvature become sensitive to pocket polarization, providing an additional source of temperature dependence. As our numerical results indicate, the combination of these effects can lead to a negative $d\rho/dT$. Second, electron-phonon interaction results in carrier scattering growing at temperatures above the Bloch-Grüneisen temperature, which leads to positive $d\rho/dT$ at high enough temperatures.

This behavior of the resistivity can be described phenomenologically as follows. At low temperature, the system is in the momentum-polarized ordered phase, which smoothly turns into a disordered phase through a continuous phase transition at temperature T_c. The conductivity of the system, given by Eq. (2), depends on the pocket polarization through the quantity $C(T)$, which is the band curvature weighted with the carrier momentum distribution. At very low temperature, the resistance is primarily affected by the band curvature, as the phonons are not yet thermally activated, and the scattering rate is almost a constant. Above T_c, the resistance will primarily increase due to phonon scattering, and the curvature will play a minor role. Here, we use a phenomenological temperature dependence of band curvature and scattering rate to demonstrate that at low temperature, the resistance can decrease with rising temperature. Later, in Sec. V, this behavior will be justified microscopically.

As we will see, the quantity $C(T)$ increases monotonically from $T = 0$ to $T = T_c$, where the ordered phase continuously turns into the disordered phase. This behavior can be modeled by a phenomenological dependence $C(T)$, which increases

between $T = 0$ and $T = T_c$:

$$\frac{C(T)}{C(T_c)} = \begin{cases} 1 - (1-\alpha)\left(1 - \frac{T}{T_c}\right)^2, & T < T_c \\ 1, & T \geqslant T_c, \end{cases} \quad (5)$$

with a suitable value $\alpha < 1$ defined as $\alpha = C(T=0)/C(T_c)$. The specific form of Eq. (5) does not matter so long as $C(T)$ grows monotonically. The form of Eq. (5) is chosen so that it mimics the simulation results in the microscopic models. For simplicity, we have set $C(T)/C(T_c) = 1$ above T_c, because there the temperature dependence of resistance is primarily determined by the phonon scattering. The exact temperature dependence of $C(T)$ obtained microscopically will be established below.

In addition to the band curvature, we must account for the temperature dependence of scattering by phonons and by disorder (defects or impurities),

$$\tau^{-1}(T) = \gamma_{\text{ph}}(T) + \gamma_{\text{dis}}(T). \quad (6)$$

At leading order, the disorder scattering rate γ_{dis} is a temperature-independent constant, γ_0. The phonon scattering rate γ_{ph} is given by the Bloch-Grüneisen formula [69,71,72], which smoothly interpolates between a power law (quartic in two dimensions) below the Bloch-Grüneisen temperature $T_{\text{BG}} = \frac{2v_s \hbar k_F}{k_B}$, and a linear dependence above this temperature (here v_s is the speed of sound and $\hbar k_F$ is the Fermi momentum). In this work, we approximate it with a simple phenomenological formula that interpolates between the two regimes, $\gamma_{\text{ph}}(T) = \gamma_1[(1 + (T/T_{\text{BG}})^4]^{1/4}$, giving

$$\gamma_{\text{ph}}(T) \approx \begin{cases} \frac{\gamma_1}{4}\left(\frac{T}{T_{\text{BG}}}\right)^4, & T \ll T_{\text{BG}} \\ \gamma_1 \frac{T}{T_{\text{BG}}}, & T \gg T_{\text{BG}}. \end{cases} \quad (7)$$

Below we set $\gamma_1 = 0.1\gamma_0$, so that the phonon scattering is relatively weak in the region of phase transition.

In bilayer graphene, the typical value of the Stoner-transition temperature T_c, and the Bloch-Grüneisen temperature T_{BG} are of the order a few kelvin. So, provided that T_{BG} is not very small compared to T_c, the momentum relaxation timescale $\tau(T)$ will not significantly change across the phase transition, and the resistivity will decrease with increasing temperature. The variation of resistivity with temperature is plotted in Fig. 3(b) for several values of α (we have chosen $T_{\text{BG}} = 0.8 T_c$ throughout the paper). When $T_{\text{BG}} > T_c$, we find that the resistance continuously decreases with temperature until T_c, and increases at higher T. When $T_{\text{BG}} \lesssim T_c$, the resistance decreases with temperature at $T \leqslant T_{\text{BG}}$. Afterwards, between T_{BG} and T_c, there will be a competition between the increasing curvature (which suppresses resistance), and the increasing phononic scattering (which enhances resistance). After reaching T_c, the resistance will increase with temperature. It is to be noted that this behavior occurs in the metallic regime and at low temperature. The decrease in resistance occurs due to the decreased (average) curvature of the conduction band, which is very different from the phenomena observed in semiconductors, where an initial rise in resistance due to phonon scattering is followed by resistance dropping because the conduction band becomes thermally accessible at higher temperatures.
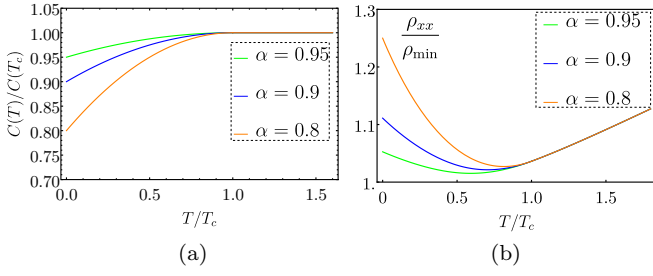
FIG. 3. (a) Band curvature of the ordered state $C(T)$ scaled by $C(T_c)$ in the phenomenological model, Eq. (5), for $\alpha = 0.8$ (orange curve), 0.9 (blue curve), and 0.95 (green curve), respectively. Here α denotes the ratio $C(T=0)/C(T=T_c)$ [see Eq. (5)]. (b) Plots for resistivity [scaled by the minimum resistivity, which is of the order $\sim \hbar^2 \gamma_0 / ne^2 C(T_c)$] of the phenomenological model for the values of α as in part (a). Parameter values used are given in Sec. III. The resistance initially decreases due to increase in average band curvature, and subsequently increases linearly due to phonon scattering.

IV. MICROSCOPIC FORMALISM

Here we introduce a microscopic approach that describes pocket-polarized order arising due to carrier flocking in momentum space governed by electron exchange interaction [61]. Under a generalized Stoner mean field, the instability that leads to pocket asymmetry and pocket polarization is analogous to spin polarization instability in the Stoner magnetism. We will consider Hamiltonians of the form

$$H = \sum_{\boldsymbol{k},\sigma} \varepsilon_{\boldsymbol{k}}^0 c_{\boldsymbol{k},\sigma}^\dagger c_{\boldsymbol{k},\sigma} + \frac{1}{2} \sum_{\substack{\boldsymbol{k},\boldsymbol{k}',\boldsymbol{q} \\ \sigma,\sigma'}} V(\boldsymbol{q}) c_{\boldsymbol{k}-\boldsymbol{q},\sigma}^\dagger c_{\boldsymbol{k}'+\boldsymbol{q},\sigma'}^\dagger c_{\boldsymbol{k}',\sigma'} c_{\boldsymbol{k},\sigma}. \quad (8)$$

Under mean-field theory, we can write the interaction term as a combination of the so-called direct (Hartree) and exchange (Fock) terms. As long as the average electron density is uniform (e.g., for Bloch waves), the Hartree term is just a constant which would not affect the electronic configurations. To the contrary, the exchange term favors carriers populating orbitals with equal spin and nearly equal momenta and can drive the instability towards carrier aggregation in momentum space. After dropping the (constant) Hartree term, we can write the mean-field free energy functional $F = E - TS$ as,

$$F[f_{\boldsymbol{k},\sigma}] = \sum_{\boldsymbol{k},\sigma} \varepsilon_{\boldsymbol{k}}^0 f_{\boldsymbol{k},\sigma} - \frac{1}{2} \sum_{\substack{\boldsymbol{k} \neq \boldsymbol{k}' \\ \sigma}} V(\boldsymbol{k} - \boldsymbol{k}') f_{\boldsymbol{k},\sigma} f_{\boldsymbol{k}',\sigma}$$
$$+ k_B T \sum_{\boldsymbol{k},\sigma} [f_{\boldsymbol{k},\sigma} \ln f_{\boldsymbol{k},\sigma} + (1 - f_{\boldsymbol{k},\sigma}) \ln(1 - f_{\boldsymbol{k},\sigma})], \quad (9)$$

where $f_{\boldsymbol{k},\sigma} = \langle c_{\boldsymbol{k},\sigma}^\dagger c_{\boldsymbol{k},\sigma} \rangle$ and the last term is the entropy contribution written in terms of the occupancy $f_{\boldsymbol{k},\sigma}$.

The functional $F[f_{\boldsymbol{k},\sigma}]$ defines a variational problem in the functional space $\{f_{\boldsymbol{k},\sigma}\}$ in which $f_{\boldsymbol{k},\sigma}$ are the variational parameters. To tackle this problem, it is convenient to work in the grand-canonical ensemble by employing the functional

$$\tilde{F}[f_{\boldsymbol{k},\sigma}] = F[f_{\boldsymbol{k},\sigma}] - \mu N, \quad (10)$$

where $N = \sum_{\boldsymbol{k},\sigma} f_{\boldsymbol{k},\sigma}$ and μ is a Lagrange multiplier that fixes the density N. To minimize the free energy, we consider the saddle-point conditions $\delta \tilde{F}/\delta f_{\boldsymbol{k},\sigma} = 0$, treating $f_{\boldsymbol{k},\sigma}$ as independent variables in the functional space. After some algebra the saddle point conditions yield coupled mean-field equations (3) and (4), which describe the critical points of the functional $\tilde{F}$. We use iterations [84] to self-consistently solve these equations (for a single spin species) to determine the system ground state.

The unique aspect of the pocket-polarized states is spontaneous symmetry breaking. Normally, in the Landau Fermi-liquid framework, the problem of interacting fermions features a single ground state, representing a Fermi sea defined by the band dispersion $\varepsilon_{\boldsymbol{k},\sigma}$ renormalized by Fermi-liquid interactions but retaining the symmetry of the free-particle band. The self-consistent equations describing such ground states, derived from the Fermi-liquid theory, are essentially the same as our mean-field equations (3) and (4). At not-too-strong interactions $V(\boldsymbol{k} - \boldsymbol{k}')$ or at elevated temperatures, these equations have a self-consistent solution representing a Fermi sea that has the point symmetry group identical to that of the free-particle band dispersion. For a single valley of graphene bilayer, K or K', perturbed by a trigonal warping interaction, it is the discrete symmetry group isomorphic to the C_{3v} group, comprising threefold rotations as well as three valley-preserving operations representing mirror symmetries σ_v followed by time reversal.

At a larger interaction strength or at a lower temperature, the self-consistent equations acquire multiple solutions, including three solutions describing broken-symmetry pocket-polarized states forming an orbit of the generalized C_{3v} group and one solution describing a symmetry-unbroken unpolarized state. Conceivably, there are two scenarios for these states to emerge from a symmetry-unbroken state upon changing the interaction strength or varying temperature. One scenario is when the broken-symmetry solutions, when they first appear, have energies higher than the symmetry-unbroken state. Another scenario is when the broken-symmetry states, when they first appear, are the ground states, whereas the symmetry-unbroken state is a metastable state. In the first case, as the interaction strength increases or temperature decreases, the broken symmetry state emerges abruptly through a type-I transition, whereas in the second case it emerges continuously through a type-II transition. In our simulations, described below, the type-II transition scenario is observed upon varying temperature, whereas a type-I transition is seen upon varying carrier density or the interaction strength.

Determining fixed points of Eqs. (3) and (4) corresponding to symmetry-unbroken and symmetry-broken states was done by the method of repeated iterations described below, which was found to converge reliably and rapidly enough. In our numerical analysis, we found it more convenient to use the canonical ensemble picture with a fixed particle density rather than the grand-canonical ensemble framework. To numerically obtain a pocket-unpolarized (symmetry-unbroken) state (metastable below T_c) we initiate the iterations with identical carrier distributions in all the pockets. This is done by filling up energy states from the bottom of each pocket, until the total number of electrons reaches the desired value. To obtain the pocket-polarized ground state with a fixed number of
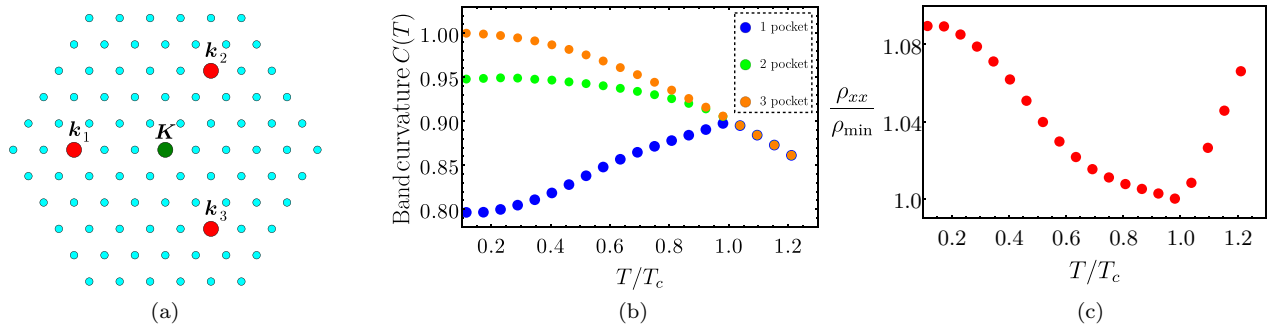
FIG. 4. (a) A triangular lattice in a hexagonal domain in momentum space, with six sites per side of hexagon, illustrating the configuration space used in the 2D model. The pockets are centered around the red points, with distance $k_0 = 3$ from the center (the K point, shown in green) of the hexagon. In the actual simulation, we have used 24 sites per side of the hexagon, with $k_0 = 12$. (b) Variation of band curvature obtained numerically for the one-pocket (blue), two-pocket (green), and three-pocket/unpolarized (orange) states of the 2D model. They become identical near T_c, until which the curvature of the one-pocket state (ground state) increases as the temperature increases. Parameter values used are given in Sec. V. (c) Temperature dependence of resistivity for the one-pocket state. In this model, the resistivity increases very quickly after reaching T_c, because of the sharp change in the slope of the band curvature [blue curve in part (c)]. It is really a very quick increase in slope rather than a nonanalytic cusp.

electrons, we initiate the iterations with an out-of-equilibrium state with a particular pocket or two pockets being populated. Afterwards, we perform iterations by calculating the renormalized band structure with Eq. (3) and using it to find the new chemical potential, such that the sum of all the occupancies $f_{k,\sigma}$ [calculated using Eq. (4) with a given temperature] equals the desired number of electrons. Plugging these new $f_{k,\sigma}$ in Eq. (3), we keep repeating this procedure until a fixed point (symmetry-broken or symmetry-unbroken) is reached. Above T_c, the equilibrium distribution becomes pocket unpolarized (symmetry unbroken), irrespective of whether the initial distribution of the iteration was pocket polarized or pocket unpolarized.

V. MODELING POCKET POLARIZATION IN 1D AND 2D SYSTEMS

Here we show how the behavior outlined in Sec. IV emerges in simple models, which resemble realistic band structures. We will start with a one-dimensional double-well band dispersion. This simple model captures the pocket-polarized order at low temperature, featuring an ordered phase that continuously turns into a disordered phase at some critical temperature T_c. At $T < T_c$, as temperature grows, the degree of pocket polarization diminishes. Simultaneously the occupancy-averaged band curvature $C(T)$ grows and Ohmic resistivity exhibits the negative $d\rho/dT$ behavior pictured in Figs. 1(d) and 4(c).

In this model, the two pockets of the noninteracting dispersion ε_k^0 are situated at some $\pm k_0$, in the region where the band is relatively flat. The form of the interaction $V(k - k')$ is chosen to favor pocket polarization. For that, the interpocket interaction must be weaker than the intrapocket interaction. These requirements are met by using the following band structure and interaction,

$$\varepsilon_k^0|_{1D} = E_0\left(\frac{k^2}{k_0^2} - 1\right)^2, \quad V(k - k') = V_0 e^{-\frac{(k-k')^2}{2q_0^2}}, \quad (11)$$

where the range of the Gaussian interaction q_0 is chosen such that the interaction is negligibly small between different pock-

ets, $q_0 \ll k_0$. For this model, by minimizing the free energy in Eq. (9), we verify that the system possesses an ordered pocket-polarized state which is thermodynamically stable below T_c. As T increases, a pocket-unpolarized state emerges at $T = T_c$ by a type-II transition, whereupon the order parameter vanishes. The order parameter describing pocket polarization can be chosen analogously to magnetization, but in terms of pocket populations rather than spins,

$$\phi_{1D} = \frac{n_R - n_L}{n_R + n_L}, \quad (12)$$

where n_L and n_R are the total electron numbers in the left and right pockets, respectively.

The numerical procedure through which an ordered state is obtained follows the description given in previous section. We initialize the system with a state which has a single pocket populated by all the electrons, and obtain the self-consistent solutions of Eq. (3) and Eq. (4) using iterations. This self-consistent solution is polarized at low temperature, and becomes unpolarized (disordered) at temperatures above some T_c. We have set $q_0 = 0.2k_0$ and used a mesh of 1001 equidistant points between $k = -1.5k_0$ to $k = 1.5k_0$, populating the system with $N = 190$ electrons so that the low-energy excitations fill up states at the bottom of an empty pocket. Since the states far away from the bottom of the pocket remain unpopulated and thermally inaccessible at the temperatures we are working with, the boundary conditions on the domain in momentum space do not affect our results, and we use open boundary conditions for convenience. For the simulation, we used dimensionless units $E_0 = 1$ and the value $V_0 = 0.004$ for the interaction strength.

For the values given above, the ordering temperature value was found to be $T_c = 0.08$. This energy scale roughly corresponds to the distance between the Fermi level in a filled pocket and the bottom of the empty pocket. As discussed in Sec. II, there is a competition between thermal excitation to the high-energy states of the filled pocket and the states at the bottom of the empty pocket in determining the temperature dependence of band curvature. To thermally excite majority of charge carriers to the bottom of the otherwise empty pocket,

we set the density such that the equilibrium distribution at $T \approx 0$ resembles Fig. 1(a), where the chemical potential is sufficiently close to the minima of the empty pocket. Then, as the temperature is increased, the empty pocket will be accessible to thermal excitation at low temperatures (without exciting very-high-energy states in the populated pocket), and the system will gradually go to the unpolarized phase. Throughout the process, the average curvature increases as the bottom of the initially unpopulated pocket becomes increasingly populated, and the resistance of the system decreases.

Now we describe how the band curvature was obtained numerically on a grid. This was done by utilizing a finite-difference method to estimate the second derivative of ε_k,

$$\Delta_k^2 \varepsilon_k|_{1D} = \frac{\varepsilon_{k+\delta k} + \varepsilon_{k-\delta k} - 2\varepsilon_k}{(\delta k)^2}. \tag{13}$$

The average curvature of the ordered and the (metastable) disordered phases are plotted in Fig. 1(c). Unlike the simplistic phenomenological model, where the curvature of the disordered phase was assumed to be a constant, here the curvature of the disordered phase decreases as temperature increases.

We use this microscopic model with Eqs. (2) and (6) to determine the resistivity vs. temperature dependence shown in Fig. 1(d). Initially, the resistivity decreases because the average curvature of the ordered state increases as the system smoothly evolves to a disordered state. Near T_c, the average curvature does not increase much, rather it begins to decrease because the system is almost disordered and the high-energy states begin to be thermally populated, see Fig. 1(c). Eventually, the phonon contribution becomes appreciable at $T > T_{BG}$, which causes an almost linear increase in resistivity for $T > T_c$.

In the second model, we consider a two-dimensional band structure with three pockets resembling the pockets induced by trigonal warping [64] near K/K' points in bilayer graphene. This model hosts one-pocket and two-pocket polarized phases at low temperature, which continuously turn into a disordered (unpolarized) phase at some T_c.

Here, the relevant order parameter $\boldsymbol{D}_k$ is the (dimensionless) dipole moment of electrons in the momentum space, measured from the $\boldsymbol{K}$ point,

$$\boldsymbol{D}_k = \frac{\sum_k (\boldsymbol{k} - \boldsymbol{K}) f_{\boldsymbol{k}}}{\sum_k k_0 f_{\boldsymbol{k}}}, \tag{14}$$

where k_0 is the distance of the center of the pockets from the $\boldsymbol{K}$ point. The direction and magnitude of this order parameter vector indicates the pockets which have been polarized as well as the nature of the polarization (i.e., one-pocket or two-pocket state). By construction, the fully polarized one-pocket state has $|\boldsymbol{D}_k| = 1$, the two-pocket polarized state has $|\boldsymbol{D}_k| = 0.5$, and the order parameter is 0 for the unpolarized state. As we obtain the equilibrium state at a particular temperature (iterating from a one-pocket or two-pocket polarized initial state), its dipole moment smoothly goes to zero, and that is how the critical temperature was estimated.

We use the following band structure and interaction:

$$\varepsilon_k^0|_{2D} = -E_0 \sum_{i=1}^{3} e^{-(\boldsymbol{k} - \boldsymbol{k}_i)^2/2q_1^2},$$

$$V(\boldsymbol{k} - \boldsymbol{k}') = V_0 e^{-(\boldsymbol{k} - \boldsymbol{k}')^2/2q_0^2}, \tag{15}$$

where $\boldsymbol{k}_1 = k_0(-1, 0)$ and $\boldsymbol{k}_{2,3} = k_0(\frac{1}{2}, \pm\frac{\sqrt{3}}{2})$ are the centers of the three pockets of radius q_1, symmetrically placed on the vertices of an equilateral triangle.

This Hamiltonian was implemented on a triangular lattice in the momentum space [see Fig. 4(a)], centered around the $\boldsymbol{K}$ point [which is also the center of the $(\boldsymbol{k}_1, \boldsymbol{k}_2, \boldsymbol{k}_3)$ triangle]. We use a triangular lattice so that all three pockets are equivalent and the discretized problem respects the trigonal symmetry. Similar to the previous model, we use open boundary conditions, because the states at the boundary remained unpopulated in the range of electron densities and temperatures we considered. Parameter values used in our simulation were $E_0 = 1$, $V_0 = 0.01$, $k_0 = 12$, $q_1 = 4$, $q_0 = 6$, and we set $k_B = 1$.

The results discussed below were obtained for a hexagonal domain with trigonal symmetry, with the total of 24 sites per side of the hexagon [see Fig. 4(a)]. The electron density was such that in the one-pocket polarized phase at $T \approx 0$, the chemical potential would be very close to the minima of the unoccupied pockets. The array within the hexagon was populated with $N = 82$ electrons so that this condition is satisfied. We find that as the temperature is increased while keeping the electron number fixed, the pocket-polarized phase gradually melts into the disordered phase, and the resistivity decreases. In addition to the one-pocket polarized and pocket-unpolarized states, a two-pocket polarized state can also be considered. For this particular model, the ground state remains one-pocket polarized at low temperature, and the two-pocket polarized state (as well as the pocket-unpolarized state) is metastable. As temperature is increased, the one-pocket and two-pocket states gradually transform into the unpolarized state, with pocket polarization disappearing at a temperature T_c.

In these simulations, the band curvature was evaluated using a discrete lattice-Laplacian implemented on the triangular lattice,

$$\Delta_k^2 \varepsilon_k|_{2D} = \frac{2}{3} \frac{\sum_{\langle k' \rangle} \varepsilon_{k'} - 6\varepsilon_k}{(\delta k)^2}, \tag{16}$$

where $\sum_{\langle k' \rangle}$ denotes the sum over the six nearest neighbors of $\boldsymbol{k}$, with δk the distance between nearest neighbors.

The resulting resistivity vs. temperature dependence is displayed in Fig. 4(c). The resistivity steadily decreases until it reaches T_{BG} because the momentum-averaged curvature decreases in this regime, and the phonon scattering remains negligible. Afterwards, between T_{BG} and T_c, there is a competition between the increasing curvature and the phonon scattering, and after reaching T_c, the resistance increases linearly.

VI. SWITCHING INDUCED BY ELECTRIC FIELD

Here we consider pocket polarization switching occurring in the nonlinear current-field response regime. Upon the application of a spatially uniform and time-independent electric field, the whole Fermi sea begins to drift in the direction opposite to the electric field and the relaxation mechanism tries to restore the equilibrium distribution. The net result of this competition is that the Fermi sea is displaced from

its equilibrium position in the steady state [69]. This can be modeled with the Boltzmann transport equation,

$$\frac{\partial f}{\partial t} + \frac{d\boldsymbol{r}}{dt} \cdot \frac{\partial f}{\partial \boldsymbol{r}} + \frac{d\boldsymbol{k}}{dt} \cdot \frac{\partial f}{\partial \boldsymbol{k}} = -\frac{f - f^0}{\tau}, \qquad (17)$$

where f is the actual nonequilibrium distribution, whereas f_0 is the equilibrium distribution defined as a Fermi function of the self-consistent energy ε_k, a quantity that accounts for the Fermi-liquid interactions with the carrier distribution perturbed by electric field. In the absence of electric field, the self-consistent energy and the equilibrium distribution are given by Eqs. (3) and (4). Here, these expressions will be modified as discussed below [Eqs. (22a) and (22b)].

This approach represents a generalization of the self-consistent relations introduced in the Fermi-liquid theory to an out-of-equilibrium regime. Accordingly, the quasiparticle velocity in the streaming term should be taken as momentum gradient of the self-consistent energy, $\frac{d\boldsymbol{r}}{dt} = \frac{1}{\hbar}\nabla_k \varepsilon_k$. However, for the spatially uniform solutions considered below the streaming term vanishes. We note that our collision term, which describes relaxation to the self-consistent equilibrium distribution, agrees with the requirements of the Fermi-liquid theory [85,86]. Here, for simplicity, we employ the relaxation time approximation, and assume that the relaxation timescale is momentum independent.

In the steady state, $\frac{\partial f}{\partial t} = 0$, and $\frac{\partial f}{\partial \boldsymbol{r}} = 0$ due to spatial homogeneity. Also, $\frac{d\boldsymbol{k}}{dt} = -\frac{e\boldsymbol{E}}{\hbar}$ from the semiclassical equations of motion, where the charge of an electron is $-e$. Then, the equation reduces to

$$f(\boldsymbol{k}) - \frac{e\tau}{\hbar}\boldsymbol{E} \cdot \frac{\partial f(\boldsymbol{k})}{\partial \boldsymbol{k}} = f^0(\boldsymbol{k}). \qquad (18)$$

This equation has a formal solution,

$$f(\boldsymbol{k}) = \frac{1}{1 - \frac{e\tau}{\hbar}\boldsymbol{E} \cdot \frac{\partial}{\partial \boldsymbol{k}}} \cdot f^0(\boldsymbol{k}). \qquad (19)$$

To evaluate it, either the operator $\frac{1}{1 - \frac{e\tau}{\hbar}\boldsymbol{E} \cdot \frac{\partial}{\partial \boldsymbol{k}}}$ can be written as a Taylor series in $\boldsymbol{E} \cdot \frac{\partial}{\partial \boldsymbol{k}}$, or more formally, it can be evaluated using Fourier transforms, giving

$$f(\boldsymbol{k}) = \int_0^\infty ds\, e^{-s} f^0(\boldsymbol{k} + s\boldsymbol{E}\tau/\hbar), \qquad (20)$$

where s is an auxiliary integration variable.

At linear order in the electric field, the solution takes the form

$$f(\boldsymbol{k}) \approx f^0(\boldsymbol{k}) + \frac{e\tau}{\hbar}\boldsymbol{E} \cdot \frac{\partial f^0(\boldsymbol{k})}{\partial \boldsymbol{k}} \approx f^0(\boldsymbol{k} + e\boldsymbol{E}\tau/\hbar), \quad (21)$$

that is, the steady-state Fermi distribution f will be a displaced version of the equilibrium Fermi distribution f^0, as described above. If we take a pocket-polarized state, apply an electric field in the appropriate direction, and keep increasing its magnitude, at some point the displaced Fermi sea may abruptly switch, resulting in all the electrons shifting to another pocket. Since a finite electric field is required for the switching, the initial state cannot be restored by decreasing the magnitude of the electric field, or by the application of a small electric field in the opposite direction. Experimentally, such memory

effects and history-dependent behavior in the transport properties may be observed by turning on a strong in-plane electric field, or by running high currents. These results, obtained here for a simple model, are expected to describe transport in a bilayer (or multilayer) graphene or transition-metal dichalcogenides (TMD) sample that hosts multiple Fermi pockets induced by trigonal warping [22,23,61]. The switching behavior, which is a consequence of pocket polarization assisted by an applied E field, may be used as an experimental probe for delineating pocket polarization from alternative mechanisms of negative $d\rho/dT$.

To model the switching effect, we modify the self-consistent equations (3) and (4) as follows. The exchange energy will depend on the field-induced steady-state distribution, modeled as the shifted equilibrium distribution. as discussed above. Namely, the coupled mean-field equations (3) and (4) must be replaced with the three equations

$$\varepsilon_{\boldsymbol{k},\sigma} = \varepsilon_{\boldsymbol{k}}^0 - \sum_{\boldsymbol{k}' \neq \boldsymbol{k}} V(\boldsymbol{k} - \boldsymbol{k}') f_{\boldsymbol{k}',\sigma}, \qquad (22a)$$

$$f_{\boldsymbol{k},\sigma} = f_{\boldsymbol{k}+e\boldsymbol{E}\tau/\hbar,\sigma}^0, \quad f_{\boldsymbol{k},\sigma}^0 = \frac{1}{e^{\beta(\varepsilon_{\boldsymbol{k},\sigma}-\mu)}+1}. \qquad (22b)$$

To numerically solve these equations, we use the 1D model [Eq. (11)] with $E_0 = 1$, $k_0 = 1$, $V_0 = 0.01$, $q_0 = 0.2$, $k_B T/E_0 = 0.2$. We use the mesh of 2001 equidistant points between $k = -3k_0$ to $k = 3k_0$, and populating it with $N = 200$ electrons. We initiate the iterations with an equilibrium distribution polarized in the right (red curve in Fig. 2) as well as the left pocket (blue curve in Fig. 2), and in each case obtain a field-induced steady-state distribution.

To clarify the underlying physics, consider the evolution of the right pocket-polarized initial state. Under the application of a small positive electric field, the steady-state distribution remains polarized at the same pocket, but as the electric field is increased, the distribution immediately switches to the left pocket, and the pocket polarization $\phi_{1D} = (n_R - n_L)/(n_R + n_L)$ discontinuously jumps from $+1$ to -1. The effect has been illustrated in Fig. 2, where the switching occurs at $E \approx 0.32\hbar k_0/e\tau$ for the parameters mentioned in the previous paragraph. If we had swept the electric field in the opposite direction from the beginning (for the same right pocket-polarized initial state), then the steady-state distribution would shift to the direction opposite to the left pocket. In this case, the system will not exhibit any switching behavior, but the pocket polarization ϕ_{1D} will gradually decrease in magnitude. Due to the displacement of the Fermi sea, the exchange energy at the minima of the filled pocket would be smaller compared to the initial state. Consequently, energy difference between the minima of the filled and the empty pockets would be smaller, and the initially empty pocket will gain some electrons due to thermal excitations. Therefore, the sign of ϕ_{1D} would remain the same, but it would decrease in magnitude, as observed in Fig. 2. The analogous and opposite effect happens with the left pocket-polarized initial state.

VII. DISCUSSION

The transport anomalies considered here, originating from pocket polarization, involve a negative temperature

dependence of resistivity predicted in the ohmic regime and polarization switching in a non-ohmic regime. We first restate the reasons for negative $d\rho/dT$ being a robust and generic property of the momentum-polarized order. At low temperatures, the electrons are predominantly scattered by disorder as the phonons are not yet thermally activated. Consequently, the resistivity of a metallic system is primarily determined by the average band curvature. Using microscopic models that mimic the pockets induced by trigonal warping in bilayer graphene and TMD, we demonstrated that the momentum-polarized ordered phase samples a greater number of states with relatively less curvature compared to its disordered counterpart, implying that the resistivity of the ordered phase will decrease with rising temperature, until the order undergoes melting. Subsequently, phonon scattering will reinstate the linear dependence of resistivity on temperature, just like conventional metals at room temperature.

Simultaneously, transport in the momentum-polarized phase features a dependence on history that leads to polarization switching. Namely, a particular momentum-polarized state can switch to a different momentum-polarized state when subjected to a strong electric field that reverses direction. This behavior is expected to give rise to hysteretic I-V characteristics that may be utilized to experimentally distinguish the mechanism of negative $d\rho/dT$ described above from other mechanisms.

A similar behavior in resistivity may be considered for the valley-polarized, and spin-polarized ordered phases at very low carrier densities. To understand the microscopic picture, consider the valley-polarized phase and, for the time being, ignore pocket polarization. At low temperature, while only one valley is polarized, the resistance will gradually increase with rising temperature, just like the behavior observed in ordinary metals. As T increases, at some point the bottom of the unpopulated valley will begin to be populated by thermally excited carriers. These carriers will sample the bottom part of the band where the curvature is high. The higher average curvature of the populated part of the band will bring the resistance down. Eventually, the thermal excitations will suppress valley-polarized order, and the resistance will begin to increase again. Therefore, as T grows, resistance will rise, then drop and then rise again.

A similar T dependence is expected to occur in the spin-polarized phase. Pocket polarization, if present, will make the behavior more complicated. However, it is unlikely to eliminate the nonmonotonic T dependence. However, for the scenario discussed above to be applicable at much higher density (where spin or valley-polarized phases are usually not observed), the band structure must be very different from standard bilayer graphene band structure near charge neutrality. Experimentally, the phases polarized in spin or valley have only been stabilized at low electronic density (close to charge neutrality). Negative $d\rho/dT$ may be observed if the ordered state can be stabilized at a high enough electronic density so that it will sample an appreciable number of states with negative band curvature from the high-energy necks linking the K or K' valleys, whereas the corresponding high-temperature state will sample a relatively greater number of states from the valley bottom, which has a positive band curvature. A band structure of this type is featured by biased antimonene, whose conduction band has several almost degenerate pockets [87,88] which at a low temperature may host pocket-polarized phases. Further research is required to explore the resistive behavior of these systems. The longitudinal resistivity decreasing with temperature, combined with the switching behavior can serve as a transport signature to experimentally identify momentum-polarized ordered phases.

[1] Y. Cao, V. Fatemi, S. Fang, K. Watanabe, T. Taniguchi, E. Kaxiras, and P. Jarillo-Herrero, Unconventional superconductivity in magic-angle graphene superlattices, Nature (London) **556**, 43 (2018).

[2] Y. Cao, V. Fatemi, A. Demir, S. Fang, S. L. Tomarken, J. Y. Luo, J. D. Sanchez-Yamagishi, K. Watanabe, T. Taniguchi, E. Kaxiras, R. C. Ashoori, and P. Jarillo-Herrero, Correlated insulator behaviour at half-filling in magic-angle graphene superlattices, Nature (London) **556**, 80 (2018).

[3] A. L. Sharpe, E. J. Fox, A. W. Barnard, J. Finney, K. Watanabe, T. Taniguchi, M. A. Kastner, and D. Goldhaber-Gordon, Emergent ferromagnetism near three-quarters filling in twisted bilayer graphene, Science **365**, 605 (2019).

[4] M. Serlin, C. L. Tschirhart, H. Polshyn, Y. Zhang, J. Zhu, K. Watanabe, T. Taniguchi, L. Balents, and A. F. Young, Intrinsic quantized anomalous Hall effect in a moiré heterostructure, Science **367**, 900 (2020).

[5] C. L. Tschirhart, M. Serlin, H. Polshyn, A. Shragai, Z. Xia, J. Zhu, Y. Zhang, K. Watanabe, T. Taniguchi, M. E. Huber, and A. F. Young, Imaging orbital ferromagnetism in a moiré Chern insulator, Science **372**, 1323 (2021).

[6] A. Kerelsky, L. McGilly, D. M. Kennes, L. Xian, M. Yankowitz, S. Chen, K. Watanabe, T. Taniguchi, J. Hone, C. Dean, A. Rubio, and A. N. Pasupathy, Maximized electron interactions at the magic angle in twisted bilayer graphene, Nature (London) **572**, 95 (2019).

[7] Y. Choi, J. Kemmer, Y. Peng, A. Thomson, H. Arora, R. Polski, Y. Zhang, H. Ren, J. Alicea, G. Refael, F. von Oppen, K. Watanabe, T. Taniguchi, and S. Nadj-Perge, Electronic correlations in twisted bilayer graphene near the magic angle, Nature Phys. **15**, 1174 (2019).

[8] Y. Jiang, X. Lai, K. Watanabe, T. Taniguchi, K. Haule, J. Mao, and E. Y. Andrei, Charge order and broken rotational symmetry in magic-angle twisted bilayer graphene, Nature (London) **573**, 91 (2019).

[9] Y. Cao, D. Rodan-Legrain, J. M. Park, N. F. Q. Yuan, K. Watanabe, T. Taniguchi, R. M. Fernandes, L. Fu, and P. Jarillo-Herrero, Nematicity and competing orders in superconducting magic-angle graphene, Science **372**, 264 (2021).

[10] Y. Saito, F. Yang, J. Ge, X. Liu, T. Taniguchi, K. Watanabe, J. I. A. Li, E. Berg, and A. F. Young, Isospin Pomeranchuk effect in twisted bilayer graphene, Nature (London) **592**, 220 (2021).

[11] U. Zondiner, A. Rozen, D. Rodan-Legrain, Y. Cao, R. Queiroz, T. Taniguchi, K. Watanabe, Y. Oreg, F. von Oppen, A. Stern, E. Berg, P. Jarillo-Herrero, and S. Ilani, Cascade of phase transitions and Dirac revivals in magic-angle graphene, Nature (London) **582**, 203 (2020).

[12] A. Rozen, J. M. Park, U. Zondiner, Y. Cao, D. Rodan-Legrain, T. Taniguchi, K. Watanabe, Y. Oreg, A. Stern, E. Berg, P. Jarillo-Herrero, and S. Ilani, Entropic evidence for a Pomeranchuk effect in magic-angle graphene, Nature (London) **592**, 214 (2021).

[13] Y. Choi, H. Kim, Y. Peng, A. Thomson, C. Lewandowski, R. Polski, Y. Zhang, H. Singh Arora, K. Watanabe, T. Taniguchi, J. Alicea, and S. Nadj-Perge, Correlation-driven topological phases in magic-angle twisted bilayer graphene, Nature (London) **589**, 536 (2021).

[14] A. T. Pierce, Y. Xie, J. M. Park, E. Khalaf, S. H. Lee, Y. Cao, D. E. Parker, P. R. Forrester, S. Chen, K. Watanabe, T. Taniguchi, A. Vishwanath, P. Jarillo-Herrero, and A. Yacoby, Unconventional sequence of correlated Chern insulators in magic-angle twisted bilayer graphene, Nature Phys. **17**, 1210 (2021).

[15] N. J. Zhang, J.-X. Lin, D. V. Chichinadze, Y. Wang, K. Watanabe, T. Taniguchi, L. Fu, and J. I. A. Li, Angle-resolved transport nonreciprocity and spontaneous symmetry breaking in twisted trilayer graphene, Nat. Mater. **23**, 356 (2024).

[16] Z. Lu, T. Han, Y. Yao, A. P. Reddy, J. Yang, J. Seo, K. Watanabe, T. Taniguchi, L. Fu, and L. Ju, Fractional quantum anomalous Hall effect in multilayer graphene, Nature **626**, 759 (2024).

[17] Y. Lee, S. Che, J. Velasco Jr., X. Gao, Y. Shi, D. Tran, J. Baima, F. Mauri, M. Calandra, M. Bockrath, and C. N. Lau, Nano Lett. **22**, 5094 (2022)

[18] H. Zhou, T. Xie, A. Ghazaryan, T. Holder, J. R. Ehrets, E. M. Spanton, T. Taniguchi, K. Watanabe, E. Berg, M. Serbyn, and A. F. Young, Half- and quarter-metals in rhombohedral trilayer graphene, Nature (London) **598**, 429 (2021).

[19] H. Zhou, L. Holleis, Y. Saito, L. Cohen, W. Huynh, C. L. Patterson, F. Yang, T. Taniguchi, K. Watanabe, and A. F. Young, Isospin magnetism and spin-polarized superconductivity in Bernal bilayer graphene, Science **375**, 774 (2022).

[20] S. C. de la Barrera, S. Aronson, Z. Zheng, K. Watanabe, T. Taniguchi, Q. Ma, P. Jarillo-Herrero, and R. Ashoori, Cascade of isospin phase transitions in Bernal bilayer graphene at zero magnetic field, Nat. Phys. **18**, 771 (2022).

[21] H. Chen, A. Arora, J. C. W. Song, and K. P. Loh, Gate-tunable anomalous Hall effect in Bernal tetralayer graphene, Nature Commun. **14**, 7925 (2023).

[22] A. M. Seiler, F. R. Geisenhof, F. Winterer, K. Watanabe, T. Taniguchi, T. Xu, F. Zhang, and R. T. Weitz, Quantum cascade of correlated phases in trigonally warped bilayer graphene, Nature (London) **608**, 298 (2022).

[23] J.-X. Lin, Y. Wang, N. J. Zhang, K. Watanabe, T. Taniguchi, L. Fu, and J. I. A. Li, Spontaneous momentum polarization and diodicity in Bernal bilayer graphene, arXiv:2302.04261.

[24] Y. Zhang, R. Polski, A. Thomson, E. Lantagne-Hurtubise, C. Lewandowski, H. Zhou, K. Watanabe, T. Taniguchi, J. Alicea, and S. Nadj-Perge, Enhanced superconductivity in spin–orbit proximitized bilayer graphene, Nature (London) **613**, 268 (2023).

[25] J. M. B. Lopes dos Santos, N. M. R. Peres, and A. H. Castro Neto, Graphene bilayer with a twist: Electronic structure, Phys. Rev. Lett. **99**, 256802 (2007).

[26] E. J. Mele, Commensuration and interlayer coherence in twisted bilayer graphene, Phys. Rev. B **81**, 161405(R) (2010).

[27] E. Suárez Morell, J. D. Correa, P. Vargas, M. Pacheco, and Z. Barticevic, Flat bands in slightly twisted bilayer graphene: Tight-binding calculations, Phys. Rev. B **82**, 121407(R) (2010).

[28] R. Bistritzer and A. H. MacDonald, Moiré bands in twisted double-layer graphene, Proc. Natl. Acad. Sci. USA **108**, 12233 (2011).

[29] F. Guinea and N. R. Walet, Electrostatic effects, band distortions, and superconductivity in twisted graphene bilayers, Proc. Natl. Acad. Sci. USA **115**, 13174 (2018).

[30] H. Isobe, N. F. Q. Yuan, and L. Fu, Unconventional Superconductivity and Density Waves in Twisted Bilayer Graphene, Phys. Rev. X **8**, 041041 (2018).

[31] V. Kozii, H. Isobe, J. W. F. Venderbos, and L. Fu, Nematic superconductivity stabilized by density wave fluctuations: Possible application to twisted bilayer graphene, Phys. Rev. B **99**, 144507 (2019).

[32] C. Xu and L. Balents, Topological superconductivity in twisted multilayer graphene, Phys. Rev. Lett. **121**, 087001 (2018).

[33] Y.-P. Lin and R. M. Nandkishore, Chiral twist on the high-Tc phase diagram in moiré heterostructures, Phys. Rev. B **100**, 085136 (2019).

[34] J. Kang and O. Vafek, Strong coupling phases of partially filled twisted bilayer graphene narrow bands, Phys. Rev. Lett. **122**, 246401 (2019).

[35] M. Xie and A. H. MacDonald, Nature of the correlated insulator states in twisted bilayer graphene, Phys. Rev. Lett. **124**, 097601 (2020).

[36] M. Ochi, M. Koshino, and K. Kuroki, Possible correlated insulating states in magic-angle twisted bilayer graphene under strongly competing interactions, Phys. Rev. B **98**, 081102(R) (2018).

[37] K. Seo, V. N. Kotov, and B. Uchoa, Ferromagnetic Mott state in twisted graphene bilayers at the magic angle, Phys. Rev. Lett. **122**, 246402 (2019).

[38] F. Wu and S. Das Sarma, Ferromagnetism and superconductivity in twisted double bilayer graphene, Phys. Rev. B **101**, 155149 (2020).

[39] F. Wu and S. Das Sarma, Collective excitations of quantum anomalous Hall ferromagnets in twisted bilayer graphene, Phys. Rev. Lett. **124**, 046403 (2020).

[40] J. F. Dodaro, S. A. Kivelson, Y. Schattner, X. Q. Sun, and C. Wang, Phases of a phenomenological model of twisted bilayer graphene, Phys. Rev. B **98**, 075154 (2018).

[41] S. Liu, E. Khalaf, J. Y. Lee, and A. Vishwanath, Nematic topological semimetal and insulator in magic angle bilayer graphene at charge neutrality, Phys. Rev. Res. **3**, 013033 (2021).

[42] N. Bultinck, S. Chatterjee, and M. P. Zaletel, Mechanism for anomalous Hall ferromagnetism in twisted bilayer graphene, Phys. Rev. Lett. **124**, 166601 (2020).

[43] A. Fischer, Z. A. H. Goodwin, A. A. Mostofi, J. Lischner, D. M. Kennes, and L. Klebl, Unconventional superconductivity in magic-angle twisted trilayer graphene, npj Quantum Mater. **7**, 5 (2022).

[44] Z. Dong, A. S. Patri, and T. Senthil, Theory of fractional quantum anomalous Hall phases in pentalayer rhombohedral graphene moiré structures, arXiv:2311.03445.

[45] B. Zhou, H. Yang, and Y.-H. Zhang, Fractional quantum anomalous Hall effects in rhombohedral multilayer graphene in the moiréless limit and in Coulomb imprinted superlattice, arXiv:2311.04217.

[46] J. Dong, T. Wang, T. Wang, T. Soejima, M. P. Zaletel, A. Vishwanath, and D. E. Parker, Anomalous Hall crystals in Rhombohedral multilayer graphene I: Interaction-driven Chern bands and fractional quantum Hall states at zero magnetic field, arXiv:2311.05568.

[47] S. Bhowmik, A. Ghosh, and U. Chandni, Emergent phases in graphene flat bands, arXiv:2309.08938.

[48] E. V. Castro, N. M. R. Peres, T. Stauber, and N. A. P. Silva, Low-density ferromagnetism in biased bilayer graphene, Phys. Rev. Lett. **100**, 186803 (2008).

[49] E. V. Castro, K. S. Novoselov, S. V. Morozov, N. M. R. Peres, J. M. B. Lopes dos Santos, J. Nilsson, F. Guinea, A. K. Geim, and A. H. Castro Neto, Electronic properties of a biased graphene bilayer, J. Phys.: Condens. Matter **22**, 175503 (2010).

[50] T. Stauber, E. V. Castro, N. A. P. Silva, and N. M. R. Peres, First-order ferromagnetic phase transition in the low electronic density regime of a biased graphene bilayer, J. Phys.: Condens. Matter **20**, 335207 (2008).

[51] H. Min, G. Borghi, M. Polini, and A. H. MacDonald, Pseudospin magnetism in graphene, Phys. Rev. B **77**, 041407(R) (2008).

[52] R. Nandkishore and L. Levitov, Flavor symmetry and competing orders in gilayer graphene, arXiv:1002.1966.

[53] V. Cvetkovic, R. E. Throckmorton, and O. Vafek, Electronic multicriticality in bilayer graphene, Phys. Rev. B **86**, 075467 (2012).

[54] R. E. Throckmorton and S. Das Sarma, Quantum multicriticality in bilayer graphene with a tunable energy gap, Phys. Rev. B **90**, 205407 (2014).

[55] J. Jung, M. Polini, and A. H. MacDonald, Persistent current states in bilayer graphene, Phys. Rev. B **91**, 155423 (2015).

[56] Y.-Z. Chou, F. Wu, J. D. Sau, and S. Das Sarma, Acoustic-phonon-mediated superconductivity in Bernal bilayer graphene, Phys. Rev. B **105**, L100503 (2022).

[57] E. V. Gorbar, V. P. Gusynin, V. A. Miransky, and I. A. Shovkovy, Broken symmetry $\nu = 0$ quantum Hall states in bilayer graphene: Landau level mixing and dynamical screening, Phys. Rev. B **85**, 235460 (2012).

[58] F. Zhang and A. H. MacDonald, Distinguishing spontaneous quantum Hall states in bilayer graphene, Phys. Rev. Lett. **108**, 186804 (2012).

[59] M. Kharitonov, Antiferromagnetic state in bilayer graphene, Phys. Rev. B **86**, 195435 (2012).

[60] A. Ghazaryan, T. Holder, M. Serbyn, and E. Berg, Unconventional superconductivity in systems with annular Fermi surfaces: Application to rhombohedral trilayer graphene, Phys. Rev. Lett. **127**, 247001 (2021).

[61] Z. Dong, M. Davydova, O. Ogunnaike, and L. Levitov, Isospin- and momentum-polarized orders in bilayer graphene, Phys. Rev. B **107**, 075108 (2023).

[62] M. Koshino and E. McCann, Trigonal warping and Berry's phase $N\pi$ in ABC-stacked multilayer graphene, Phys. Rev. B **80**, 165409 (2009).

[63] F. Zhang, B. Sahu, H. Min, and A. H. MacDonald, Band structure of ABC-stacked graphene trilayers, Phys. Rev. B **82**, 035409 (2010).

[64] E. McCann and M. Koshino, The electronic properties of bilayer graphene, Rep. Prog. Phys. **76**, 056503 (2013).

[65] A. F. Young (private communication).

[66] C. L. Tschirhart, E. Redekop, L. Li, T. Li, S. Jiang, T. Arp, O. Sheekey, T. Taniguchi, K. Watanabe, M. E. Huber, K. F. Mak, J. Shan, and A. F. Young, Intrinsic spin Hall torque in a moiré Chern magnet, Nat. Phys. **19**, 807 (2023).

[67] Y. Su and S.-Z. Lin, Current-induced reversal of anomalous Hall conductance in twisted bilayer graphene, Phys. Rev. Lett. **125**, 226401 (2020).

[68] L. Chua, Memristor-The missing circuit element, in *IEEE Transactions on Circuit Theory* (IEEE, 1971), Vol. 18, pp. 507–519.

[69] N. W. Ashcroft and N. D. Mermin, *Solid State Physics* (Academic Press, New York, 1970).

[70] A. M. Seiler, N. Jacobsen, M. Statz, N. Fernandez, F. Falorsi, K. Watanabe, T. Taniguchi, Z. Dong, L. S. Levitov, and R. T. Weitz, Probing the tunable multi-cone bandstructure in Bernal bilayer graphene, arXiv:2311.10816.

[71] H. L. Stormer, L. N. Pfeiffer, K. W. Baldwin, and K. W. West, Observation of a Bloch-Grüneisen regime in two-dimensional electron transport, Phys. Rev. B **41**, 1278(R) (1990).

[72] E. H. Hwang and S. Das Sarma, Acoustic phonon scattering limited carrier mobility in two-dimensional extrinsic graphene, Phys. Rev. B **77**, 115449 (2008).

[73] M. E. Fisher and J. S. Langer, Resistive anomalies at magnetic critical points, Phys. Rev. Lett. **20**, 665 (1968).

[74] A. Gold and V. T. Dolgopolov, Temperature dependence of the conductivity for the two-dimensional electron gas: Analytical results for low temperatures, Phys. Rev. B **33**, 1076 (1986).

[75] B. L. Altshuler and D. L. Maslov, Theory of metal-insulator transitions in gated semiconductors, Phys. Rev. Lett. **82**, 145 (1999).

[76] B. L. Altshuler, D. L. Maslov, and V. M. Pudalov, Metal-insulator transition in 2D: Resistance in the critical region, Physica E **9**, 209 (2001).

[77] G. Zala, B. N. Narozhny, and I. L. Aleiner, Interaction corrections at intermediate temperatures: Longitudinal conductivity and kinetic equation, Phys. Rev. B **64**, 214204 (2001).

[78] R. N. Gurzhi, Hydrodynamic effects in solids at low temperature, Sov. Phys. Usp. **11**, 255 (1968).

[79] A. V. Andreev, S. A. Kivelson, and B. Spivak, Hydrodynamic description of transport in strongly correlated electron systems, Phys. Rev. Lett. **106**, 256804 (2011).

[80] H. Guo, E. Ilseven, G. Falkovich, and L. Levitov, Higher-than-ballistic conduction of viscous electron flows, Proc. Natl. Acad. Sci. USA **114**, 3068 (2017).

[81] P. Ledwith, H. Guo, A. Shytov, and L. Levitov, Tomographic Dynamics and Scale-Dependent Viscosity in 2D Electron Systems, Phys. Rev. Lett. **123**, 116601 (2019).

[82] R. Krishna Kumar, D. A. Bandurin, F. M. D. Pellegrino, Y. Cao, A. Principi, H. Guo, G. H. Auton, M. Ben Shalom, L. A. Ponomarenko, G. Falkovich, K. Watanabe, T. Taniguchi, I. V. Grigorieva, L. S. Levitov, M. Polini, and A. K. Geim, Superballistic flow of viscous electron fluid through graphene constrictions, Nature Phys. **13**, 1182 (2017).

[83] L. V. Ginzburg, C. Gold, M. P. Roosli, C. Reichl, M. Berl, W. Wegscheider, Th. Ihn, and K. Ensslin, Superballistic electron flow through a point contact in a Ga[Al]As heterostructure, Phys. Rev. Res. **3**, 023033 (2021).

[84] The programs written in JULIA for calculating the self-consistent solutions of Eq. (3) and Eq. (4), as well as Eq. (22) are available at https://github.com/archisman-panigrahi/electronic-ordering-signature-resistance-codes.

[85] D. Pines and P. Nozieres, *The Theory of Quantum Liquids, Vol. 1: Normal Fermi Liquids* (Addison-Wesley, Reading, MA, 1988).

[86] L. P. Pitaevskii and E. M. Lifshitz, *Physical Kinetics*, Vol. 10 (Pergamon Press, Oxford, 1981).

[87] G. Wang, R. Pandey, and S. P. Karna, Atomically thin group V elemental films: Theoretical investigations of antimonene allotropes, ACS Appl. Mater. Interfaces **7**, 11490 (2015).

[88] R. Roldán, L. Chirolli, E. Prada, J. A. Silva-Guillén, P. San-Jose, and F. Guinea, Theory of 2D crystals: Graphene and beyond, Chem. Soc. Rev. **46**, 4387 (2017).